



# Quantum-enhanced phase imaging without coincidence counting

A. NICHOLAS BLACK,<sup>1,\*</sup>  LONG D. NGUYEN,<sup>1</sup>  BORIS BRAVERMAN,<sup>2</sup> KEVIN T. CRAMPTON,<sup>3</sup> JAMES E. EVANS,<sup>3,4</sup> AND ROBERT W. BOYD<sup>1,5</sup> 

<sup>1</sup>Department of Physics and Astronomy, University of Rochester, Rochester, New York 14627, USA

<sup>2</sup>QuEra Computing Inc., Boston, Massachusetts 02135, USA

<sup>3</sup>Pacific Northwest National Laboratory, Environmental Molecular Sciences Laboratory, Richland, Washington 99354, USA

<sup>4</sup>School of Biological Sciences, Washington State University, Pullman, Washington 99164, USA

<sup>5</sup>Department of Physics, University of Ottawa, Ottawa, Ontario K1N 6N5, Canada

\*ablack18@ur.rochester.edu

Received 6 December 2022; revised 6 June 2023; accepted 19 June 2023; published 19 July 2023

**Quantitative phase imaging provides a way to image transparent objects, such as biological cells, and measure their thickness. We report on a phase-imaging method that achieves twice the phase shift and approximately 1.7 times the spatial resolution of an equivalent spatially and temporally coherent classical quantitative phase-imaging system by using quantum interference between successive spontaneous parametric downconversion events in a nonlinear crystal. Furthermore, our method is approximately 1000 times faster than imaging the parametric downconversion photons in coincidence, which requires measurement times on the order of tens of hours. Our method may be useful for imaging sensitive transparent objects that require low illumination intensities at near-infrared and longer illumination wavelengths, such as photosensitive biological samples.** © 2023 Optica Publishing Group under the terms of the [Optica Open Access Publishing Agreement](#)

<https://doi.org/10.1364/OPTICA.482926>

## 1. INTRODUCTION

Before the advent of phase-contrast [1], differential interference contrast [2], and quantitative phase imaging [3–5] techniques, forming an intensity image of a phase-only object and measuring the phase imparted by that object was an outstanding problem in biological imaging. Briefly, Zernike's phase contrast method [1] relies upon destructive interference between the low and high spatial frequency content of an image, resulting in enhanced contrast near sharp features in the image. Differential interference contrast [2] relies upon interference between light that has passed through nearby points on a phase-only object, allowing the measurement of phase gradients on a phase-only object. Though these techniques are inherently stable, phase contrast and differential interference contrast modalities require extra modifications to measure the actual phase imparted by a phase-only object. Generically, quantitative phase imaging is a method to reconstruct the phase imparted to coherent light that has passed through a phase-only object by interfering it with a reference beam.

Spatially entangled photons have enabled imaging at wavelengths where cameras are inadequate [6] and with a higher resolution than classical coherent imaging [7,8]. Position-momentum entanglement has also been utilized to develop new adaptive optics schemes [9–11], and recently, new phase-imaging modalities have been developed using entangled photons. In 2019, spatially entangled photons were used to measure both amplitude and phase in low-light Fourier ptychography [12]. In 2020,

Defienne *et al.* reported a new phase-shifting holography scheme that utilized spatial and polarization entanglement [13]. Similarly, in 2021 Camphausen *et al.* demonstrated a version of differential interference contrast imaging that used polarization and spatial entanglement [14]. Induced coherence without induced emission in spontaneous parametric downconversion was employed by Lemos *et al.* to image a phase-only object that was opaque at the detection wavelength [15,16]. Lemos's paper inspired several other demonstrations and ideas based on induced-coherence imaging [17–22]. Induced coherence has also been used to perform infrared spectroscopy of gaseous samples without the use of an infrared source or infrared detection equipment [23].

In this paper, we report on a wide-field quantitative phase-imaging technique that relies upon quantum interference between sequential downconversion events in a double-passed nonlinear crystal, similar to induced coherence. As compared to an equivalent low-light fully coherent classical phase-shifting holography system, our method achieves twice the phase shift and approximately 1.7 times the spatial resolution when imaging a phase-only object. Furthermore, it is this double phase shift that separates our quantum phase imaging scheme from other induced-coherence imaging techniques [16,19,24], though the imaging photons must be detected in our scheme. Unlike quantum-enhanced differential interference contrast microscopy, our method achieves twice the phase shift [14], but the contrast in the measured phase does not come at the expense of resolution. Because the object is illuminated

with approximately 40 photons/s/ $\mu\text{m}^2$  and at a near-infrared wavelength (810 nm), our technique may be useful for imaging phase-only biological samples that are sensitive to photon flux or are prone to photobleaching, without the loss of resolution associated with imaging at longer wavelengths [25,26]. Typically, a biological object is considered phase-only if it is unstained and thin relative to the depth of focus. Importantly, this applies to live-cell imaging in various media. Though our method utilizes the strong momentum and position correlation of entangled photons produced in spontaneous parametric downconversion, detecting the photons in coincidence is not required. The field of coincidence imaging has made strides in recent years [27–29], but state-of-the-art coincidence imaging still requires tens of hours for data collection. We are able to collect all measurements necessary to generate a phase image in tens of seconds, bringing the time scale of quantum imaging closer to that of biological processes. Though our low-light imaging method does not take advantage of the signal-to-noise enhancement associated with coincidence imaging [30], it can easily accommodate coincidence imaging techniques as equipment that enables shorter acquisition times becomes more readily available [31].

## 2. BACKGROUND

The experimental setup (explained in more detail later) for generating entangled photons that interact with a phase-only object is shown in Fig. 1(a). Briefly, the method shown in Fig. 1(a) relies upon the interference between entangled photons created from spontaneous parametric downconversion of a pump beam that passes through a nonlinear crystal (BBO) twice. The momentum-representation wave function for photons created in a single spontaneous parametric downconversion event is given by [10]

$$\psi_0(\boldsymbol{\kappa}_s, \boldsymbol{\kappa}_i) = \mathcal{C} \mathcal{E}(\boldsymbol{\kappa}_s + \boldsymbol{\kappa}_i) \tilde{\chi}^{(2)}(\boldsymbol{\kappa}_s - \boldsymbol{\kappa}_i), \quad (1)$$

where  $s$  and  $i$  denote the signal and idler photons, respectively,  $\mathcal{C}$  is a constant that includes properties of the nonlinear crystal, and  $\boldsymbol{\kappa}$  represents the transverse component of the photons' wave vectors. The angular spectrum of the pump laser used to generate the signal and idler is represented by  $\mathcal{E}(\boldsymbol{\kappa}_s + \boldsymbol{\kappa}_i)$ . Its dependence on  $\boldsymbol{\kappa}_s + \boldsymbol{\kappa}_i$  reflects the conservation of transverse momentum in the downconversion process. Typically, the pump beam used to generate the signal and idler has a Gaussian angular spectrum. The nonlinear

crystal used to generate the signal and idler photons influences the two-photon wave function through  $\tilde{\chi}^{(2)}(\boldsymbol{\kappa}_s - \boldsymbol{\kappa}_i)$ , the so-called phase-matching function.  $\tilde{\chi}^{(2)}$  is the Fourier transform of the nonlinear susceptibility along the propagation of the two photons, and its dependence upon  $\boldsymbol{\kappa}_s - \boldsymbol{\kappa}_i$  results from assuming negligible walk-off of the signal and idler photons, degenerate downconversion, and the paraxial approximation. In this experiment and most others, the nonlinear susceptibility is a rectangular function in the direction of propagation. Thus, assuming a crystal of length  $\ell$  and denoting the pump wavenumber by  $k_p$ ,

$$\tilde{\chi}^{(2)}(\boldsymbol{\kappa}_s - \boldsymbol{\kappa}_i) \propto \exp[i\ell(\boldsymbol{\kappa}_s - \boldsymbol{\kappa}_i)^2/4k_p] \text{sinc}(\ell(\boldsymbol{\kappa}_s - \boldsymbol{\kappa}_i)^2/4k_p). \quad (2)$$

The two-photon wave function in the position-representation is simply the inverse Fourier transform of  $\psi_0(\boldsymbol{\kappa}_s, \boldsymbol{\kappa}_i)$ ,

$$\Phi_0(\mathbf{x}_s, \mathbf{x}_i) = \mathcal{F}^{-1}\{\psi_0(\boldsymbol{\kappa}_s, \boldsymbol{\kappa}_i)\}, \quad (3)$$

where the inverse Fourier transform, denoted  $\mathcal{F}^{-1}$ , occurs over both the  $\boldsymbol{\kappa}_s$  and  $\boldsymbol{\kappa}_i$  coordinates. In Fig. 1(a), the signal and idler modes from one pass are matched to those of the second pass, it is not possible to determine whether a detected photon was created on the first pass or the second pass through the crystal. In this case, the two-photon wave function after the second pass through the crystal is

$$\Phi_1(\mathbf{x}_s, \mathbf{x}_i) = \exp[i(\phi_{\text{obj}}(\mathbf{x}_s) + \phi_{\text{obj}}(\mathbf{x}_i))] \Phi_0(\mathbf{x}_s, \mathbf{x}_i). \quad (4)$$

If the photons described by the state in Eq. (4) pass back through the nonlinear crystal with the pump beam in such a way that the signal and idler modes from one pass are matched to those of the second pass, it is not possible to determine whether a detected photon was created on the first pass or the second pass through the crystal. In this case, the two-photon wave function after the second pass through the crystal is

$$\begin{aligned} \Phi_2(\mathbf{x}_s, \mathbf{x}_i) &= \Phi_0(\mathbf{x}_s, \mathbf{x}_i) (\exp(i\theta) + \exp[i(\phi_{\text{obj}}(\mathbf{x}_s) + \phi_{\text{obj}}(\mathbf{x}_i))]) / \sqrt{2}, \end{aligned} \quad (5)$$

where  $\theta$  is any additional phase acquired by the pump between the first and second pass. The probability of detecting only the signal photon is obtained by integrating  $|\Phi_2(\mathbf{x}_s, \mathbf{x}_i)|^2$  over the entire coordinate space of  $\mathbf{x}_i$ , i.e., calculating the marginal probability distribution of the joint probability distribution. In practice, it is easiest to perform the integration numerically. However, if

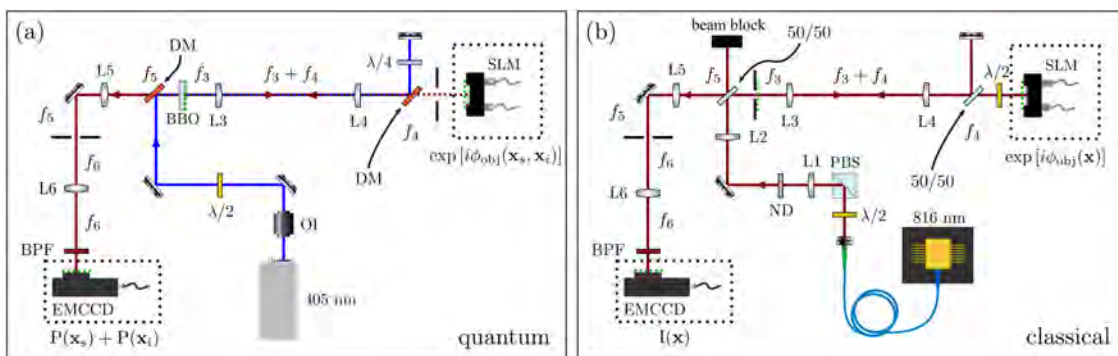


**Fig. 1.** Experimental setup for (a) quantum phase-shifting holography and (b) classical phase-shifting holography. Green dotted lines indicate conjugate image planes. 405 nm, narrow linewidth ( $<5$  MHz), 100 mW, 405 nm laser; 50/50, 50/50 beam splitter; 816 nm–33  $\mu\text{W}$ , 816 nm laser; BPF, 810  $\pm$  5 nm bandpass filter; BBO, type I beta-barium borate crystal; DM, long-pass dichroic mirror; EMCCD, electron-multiplying camera;  $f_3 = 10$  cm;  $f_4 = 30$  cm;  $f_5 = 12.5$  cm;  $f_6 = 40$  cm; L1, 10 cm lens; L2, 30 cm lens; L3, 10 cm achromatic doublet lens; L4, 30 cm achromatic doublet lens; L5, 12.5 cm lens; L6, 40 cm lens;  $\lambda/2$ , half-wave plate;  $\lambda/4$ , quarter-wave plate; ND, neutral density filters, optical density = 7; OI, optical isolator; PBS, polarizing beam splitter.

the pump is assumed to be a plane wave and the nonlinear crystal is thin enough so that  $\chi^{(2)}(\mathbf{x}_s - \mathbf{x}_i) \approx \delta(\mathbf{x}_s - \mathbf{x}_i)$ , where  $\chi^{(2)}(\mathbf{x}_s - \mathbf{x}_i) = \mathcal{F}^{-1}\{\tilde{\chi}^{(2)}(\boldsymbol{\kappa}_s - \boldsymbol{\kappa}_i)\}$ , it is possible to analytically calculate the probability of detecting only the signal photon,

$$P(\mathbf{x}_s) = \mathcal{C} (1 + \cos [2\phi_{\text{obj}}(\mathbf{x}_s) - \theta]) / \sqrt{2}. \quad (6)$$

Thus, the image formed on the electron-multiplying camera (EMCCD) in Fig. 1(a) is an interference pattern that corresponds to the phase-only object but with twice the phase shift. Equation (6) describes an ideal scenario where no losses occur to the signal or idler fields, but the visibility of interference will depend upon the product of the signal and idler losses.

The phase object can be reconstructed by employing phase-shifting holography. In classical phase-shifting holography, the light that interacted with the phase-only object interferes with a reference field, and the resulting interference pattern,  $I$ , is recorded for four different phase shifts of the reference field:  $\phi = \arg[I_0 - I_\pi + i(I_{\pi/2} - I_{3\pi/2})]$ , where the subscript on  $I$  indicates the reference phase [4]. In quantum phase-shifting holography, the reference phase is any extra phase acquired by the pump before passing through the nonlinear crystal a second time,  $\theta$  in Eq. (6). Alternatively, the phase of the pump can remain fixed while a constant phase offset is applied to the photons that interacted with the phase object. In Fig. 1(a), the reference phase is applied by the spatial light modulator (SLM) that also forms the phase object, in effect changing the global phase of the phase object. The phase is then reconstructed as follows:

$$2\phi_{\text{obj}}(\mathbf{x}_s) = \tan^{-1} \left[ \frac{P_{-\pi/4}(\mathbf{x}_s) - P_{-3\pi/4}(\mathbf{x}_s)}{P_0(\mathbf{x}_s) - P_{-\pi/2}(\mathbf{x}_s)} \right], \quad (7)$$

where the subscript on  $P$  is the value of the constant phase offset added to the SLM. Note that the absolute value of the reference phase applied to the entangled photons must be half the value used in classical phase-shifting holography, since both photons acquire the phase shift. The choice of negative phases is a matter of preference, but the particular combination of measurements used to reconstruct the phase object will depend upon the choice of reference phases and their signs. In practice, the SLM used in Fig. 1(a) is capable of phase shifts ranging from 0 to  $2\pi$  rad, so the positive representations of the phases in Eq. (7) were used, namely,  $7\pi/4$ ,  $3\pi/2$ , and  $5\pi/4$  instead of  $-\pi/4$ ,  $-\pi/2$ , and  $-3\pi/4$ , respectively. It is worth noting that phase-shifting holography with four phase shifts, like in Eq. (7), reaches the Cramer–Rao bound for phase estimation [32].

The advantage of the double phase shift can be understood by considering the phase shift imparted by an object of refractive index  $n$ . Assuming the illumination source wavenumber is given by  $k$  and the object under study has a thickness  $z$ , the phase imparted to the light is given by  $\phi_{\text{obj}} = nkz$ . The uncertainty in the thickness of the object is then

$$dz = \left| \frac{d\phi_{\text{obj}}}{nk} \right|. \quad (8)$$

If one were to use light of a higher wavenumber, then the uncertainty in the thickness of the object is smaller, provided the uncertainty in the phase remains the same. Two-photon light has an effective wavenumber of  $2k_0$ , where  $k_0$  is the wavenumber of the signal and idler photons individually. Thus, the quantum phase-shifting holography scheme in Fig. 1(a) is capable of estimating the thickness of a transparent object with half the uncertainty

of a classical scheme using coherent light of the same wavelength as the individual signal and idler photons. Furthermore, this increased sensitivity is achieved without exposing the sample to light of a shorter wavelength, which could potentially damage the object.

### 3. EXPERIMENT

The experimental setups for quantum phase-shifting holography and classical phase-shifting holography are shown in Fig. 1(a) and Fig. 1(b), respectively. In the quantum experiment, a narrow linewidth ( $<5$  MHz) 405 nm laser beam passes through an optical isolator (OI) and half-wave plate ( $\lambda/2$ ) before being directed through a 0.5-mm-long beta-barium borate crystal (BBO) by a long-pass dichroic mirror (DM). The diameter of the 405 nm pump beam at the BBO crystal is  $\sim 1$  mm. A 405 nm pump photon is converted to two 810 nm position-momentum entangled photons in the BBO crystal through degenerate type I spontaneous parametric downconversion. Both the entangled photons and the pump beam pass through the same Keplerian telescope consisting of two achromatic doublet lenses (L3 and L4) with a  $3\times$  magnification. The telescope images the output facet of the nonlinear crystal onto the active area of the SLM (green dotted line). A second long-pass DM placed after L4 splits the pump beam and entangled photons so that only the 810 nm entangled photons interact with the SLM. The SLM imprints both the phase object and constant reference phase for phase-shifting holography on the entangled photons. Accordingly, the phase of the pump is held fixed. A 1.1-cm-diameter aperture is placed between the DM and SLM to mimic the aperture of a half-wave plate just before the SLM in the classical experiment. The visibility of interference between successive downconversion events is lower than 100% because the combined transmission of L3 and L4 is  $\sim 90\%$  and because of the presence of background fluorescence. To compensate for this and recover interference visibility ( $\sim 30\%$ ), the polarization of the pump is set for imperfect phase matching before the first pass through the nonlinear crystal using a half-wave plate ( $\lambda/2$ ) and set for perfect phase matching using a double-passed quarter-wave plate ( $\lambda/4$ ) between the first and second passes through the nonlinear crystal [33]. After the entangled photons reflect from the SLM and the pump reflects from a mirror, the pump and entangled photons are recombined at the DM. They pass back through the telescope formed by L3 and L4 and through the nonlinear crystal. The first DM then splits the pump and entangled photons, and the entangled photons pass through a  $3.2\times$  telescope (L5 and L6) that images the SLM onto an EMCCD (Andor iXon 888EXF). An adjustable aperture placed a distance  $f_5 = 12.5$  cm from L5 (the Fourier plane of the SLM), limits the spatial bandwidth of the imaging system but is only engaged when comparing the resolution of the quantum and classical experiments, Fig. 3.

In the classical experiment, an  $\sim 33$   $\mu\text{W}$ , 816 nm diode laser is attenuated by a half-wave plate ( $\lambda/2$ ), polarizing beam splitter (PBS), and a series of neutral density (ND) filters with a total extinction of approximately  $10^7$ . The attenuation is set so that the photon flux incident on the object is the same as in the quantum experiment ( $\sim 40$  photons/s/ $\mu\text{m}^2$ ), as measured by the EMCCD in photon-counting mode [27,34]. Furthermore, the laser is operated near threshold to mimic the occurrence of background fluorescence created by the 405 nm pump as it passes through lenses in the quantum experiment. To do this, the laser current is

set so that the visibility of interference is the same as in the quantum experiment, which is limited by background fluorescence. The polarization is set to vertical by a PBS because the 50/50 plate beam splitter (50/50) that forms the interferometer is truly 50/50 for the vertical polarization only. The first 50/50 beam splitter serves to make the layout of the classical experiment similar to the quantum experiment. The beam is expanded to have a diameter of  $\sim 1$  mm using a Keplerian telescope with a  $3\times$  magnification (L1 and L2). The beam then passes through the same Keplerian telescope used in Fig. 1(a) consisting of two achromatic doublet lenses (L3 and L4). A 5-mm-diameter aperture is placed a distance  $f$  in front of L3 to mimic the aperture of the nonlinear crystal used in the quantum experiment (BBO). After passing through the telescope, the beam is split by a 50/50 beam splitter to form a Michelson interferometer. One arm of the Michelson interferometer is terminated by a reflective phase-only SLM that both forms the phase object ( $\phi_{\text{obj}}$ ) and introduces a constant phase offset for phase-shifting holography. The other arm is terminated by a mirror, and both arms are the same optical length. A half-wave plate placed between the 50/50 beam splitter and SLM rotates the polarization to be along the optical axis of the SLM and rotates it back to vertical after reflecting from the SLM. The beam that interacted with the SLM and the reference beam reflect back through the telescope made from L3 and L4 and the first 50/50 beam splitter before passing through another Keplerian telescope with a  $3.2\times$  magnification (L5 and L6). Like the quantum experiment, an adjustable aperture is placed in the Fourier plane of the phase object to compare the resolution of the quantum experiment with the classical experiment. The image of the active area of the SLM is then brought to the EMCCD by L6. In both the quantum and classical experiments, the phase is passively stabilized by floating the optical table and covering the beam paths with boxes to reduce air flow. The phase drift of the quantum experiment is estimated to be no greater than  $\pi/10$  over 4 min.

## 4. RESULTS

Figure 2 shows the results of a phase reconstruction experiment using classical and quantum phase-shifting holography. The phase object encoded on the SLM is shown in Fig. 2(a). A line cut through a portion of the object, Fig. 2(b), is approximately a rectangular function with a height of  $\pi/2$ . The results of classical phase-shifting holography are shown in Figs. 2(c) and 2(d). For each reference phase shift given by Eq. (7), 10 frames are averaged together. Note that the reference phases are doubled in the classical case because the classical beam does not experience a double phase shift. The EMCCD is set to have an EM gain of 1000, an exposure time of 0.02 s, and is operated in photon-counting mode. The camera settings and number of frames collected for averaging are the same in both the quantum and classical experiments. The readout time of the EMCCD sensor limits the frame rate to approximately five frames per second. The phase image in Fig. 2 agrees well with the phase object, but contains a slight astigmatism due to the use of plate-style 50/50 beam splitters in the optical path. The camera is placed in a plane where the vertical direction is in focus to make fitting to the vertical line cut (blue line) more straightforward. The line cut and fit for the classical experiment are shown in Fig. 2(d). Using maximum likelihood estimation (MLE) with the model of a rectangular function, the maximum phase shift in the line cut is estimated to be  $1.6(1)$  rad, consistent with the maximum phase shift of the encoded phase object. The uncertainty in the fit is obtained through Monte Carlo simulation using the measured intensity uncertainties at each pixel, assuming they follow a Gaussian distribution.

The results of phase imaging using quantum light are shown in Fig. 2(e), where the location of the line cut is indicated by the green line. The phase image agrees well with the encoded phase object, albeit with twice the phase shift. The astigmatism associated with the plate-style DMs is less present in the quantum experiment because they are half as thick as the 50/50 beam splitters in the

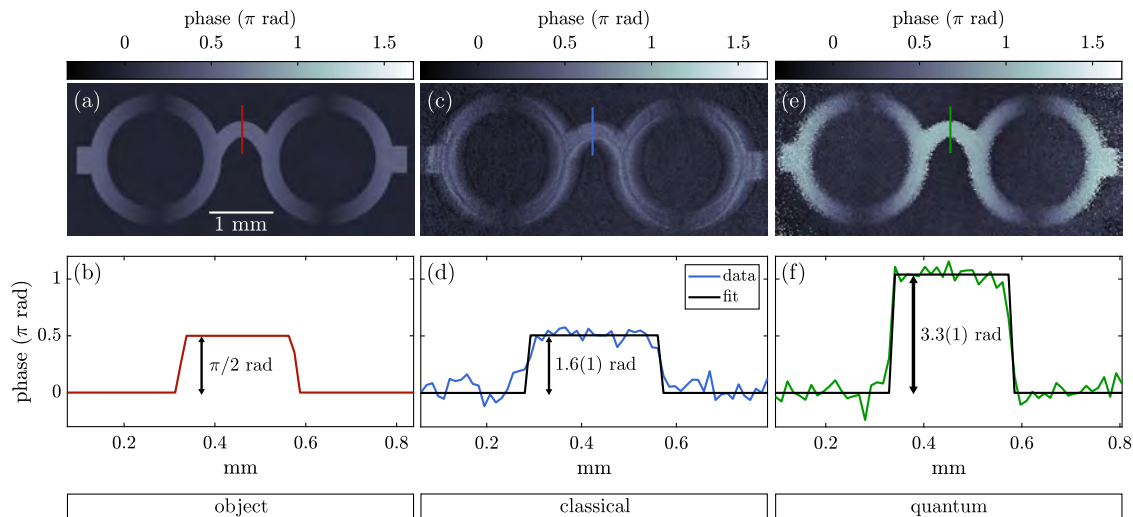


**Fig. 2.** Comparison of phase-shifting holography using classical coherent light with a wavelength of 816 nm (c) and (d) and “which crystal” quantum interference between photons with a wavelength of 810 nm (e) and (f). (a) The phase object is an illustration of round eyeglasses, and a line cut through the nosepiece (red line) is approximately a rectangular function of (b) height  $\pi/2$  rad. The result of classical phase-shifting holography is shown in (c). The ringing around the edges of the classical phase image is due to astigmatism induced by the plate beam splitters in Fig. 1(b), but the camera is placed in a plane where the vertical direction is in focus. A rectangular function is fit to a line cut through the nosepiece (blue line) using maximum likelihood estimation (d), returning a phase shift of  $1.6(1)$  rad. The result of quantum phase-shifting holography is shown in (e), and the fit to a line cut through the nosepiece (green line) is shown in (f). With a maximum phase shift of  $3.3(1)$  rad, the quantum phase-shifting holography result has approximately twice the phase shift and half the fractional uncertainty of classical phase-shifting holography.

classical experiment. The double phase shift is clearly present in the line cut, Fig. 2(f). MLE returns a maximum phase shift of  $3.3(1)$  rad, confirming the double phase shift effect. It is worth noting that quantum phase-shifting holography achieves an estimate of the phase with half the fractional uncertainty of the classical phase-shifting holography method, even though the photons that interacted with the phase object were not half the wavelength. Of course, the improvement of fractional uncertainty using quantum phase-shifting holography cannot be achieved in environments with significant mechanical instability, since the double phase shift would enhance the effect of mechanical vibrations on the phase uncertainty. The primary sources of noise in the measurement of the phase were background light and noise associated with the EM amplification in the EMCCD [27,34], rather than shot noise associated with the imaging photons. The presence of noise near the edges of the phase-object in the quantum experiment is due to phase jumps associated with the fact that the inverse tangent function operates from  $-\pi$  to  $\pi$  in MATLAB, the software used for data analysis. In principle, this can be avoided by using a phase-wrapping algorithm, but phase-wrapping algorithms tend to fail with noisy data, like that shown in Fig. 2.

Equation (6), though illustrative, implies an infinite spatial resolution. In reality, the spatial resolution of the quantum phase-shifting holography method described in Fig. 1(a) is limited by the width of the position correlation between the signal and idler photons and the apertures placed in the optical path [24,35]. A comparison of the aperture-limited resolutions for quantum and classical phase-shifting holography are shown in Fig. 3. To perform these measurements, a horizontally oriented adjustable slit was placed a distance  $f_5$  away from the lens L5 of the telescope just before the camera. The location of the slit corresponded to the Fourier plane of the phase object and nonlinear crystal. The width of the slit was fixed at 4.5 mm for both the quantum and classical experiments. A series of three equally spaced bars along the horizontal direction formed the phase object, Fig. 3(a). Each bar had a phase of  $\pi/2$  above the background, and the space between each bar was equal to the width of a single bar. The spatial frequency of the bars in the top, middle, and bottom rows of Fig. 3 were 8, 10, and 13.3 lp/mm, respectively. The aperture-limited resolution was

measured rather than the correlation-limited resolution because it is possible to increase the correlation-limited resolution by altering the magnification of the optical system between the crystal and object [24], at the expense of the field of view. Nonetheless, the correlation-limited resolution is estimated to be  $\sim 30 \mu\text{m}$  (or  $\sim 17$  lp/mm) using a crystal of length 0.5 mm and using the optical system in Fig. 1(a). The full field of view in Fig. 1(a) was limited to approximately 3 mm by the diameter of the downconversion beam. The resolution limit is assumed to be twice the standard deviation of the position correlation of the signal and idler.

The resolution measurements are shown in Fig. 3(b). Each image in Fig. 3(b) is the average of 100 frames collected by the camera with an EM gain of 213 and exposure time of 0.22 s. Furthermore, each image represents a single interferogram with the background in destructive interference and the bars in constructive interference. The three bars are clearly resolved at 8 lp/mm (top row) in both the classical (top left) and quantum experiments (top right). Extraneous fringes are present in the classical experiment due to backreflected light from lenses L3 and L4. Interestingly, these fringes do not appear in the quantum experiment because the backreflected light is not mode-matched with the entangled photons created on the second pass through the crystal. The quantum results have background noise due to broadband fluorescence created by the pump passing through lenses L3 and L4. At 10 lp/mm (middle row), the classical experiment is no longer able to resolve the three bars (middle left), but the three bars are clearly resolved in the quantum experiment (middle right). At 13.3 lp/mm (bottom row), the three bars are still resolved in the quantum experiment (bottom right) but with lower visibility than for bars at 10 lp/mm. As expected, the three bars at 13.3 lp/mm are not resolved in the classical experiment (bottom left).

The experimental results in Fig. 3(b) agree very closely with the numerical simulation; see Fig. 3(c). The simulation was performed using Fresnel propagation of the classical field and two-photon state in Eq. (1), including all apertures present in Fig. 1 [36]. After propagating the two-photon state, the marginal distribution for the signal photon was calculated to form the results in the “quantum” column of Fig. 3(c). Like the experimental results, the simulation shows that the three bars are clearly resolved for all of

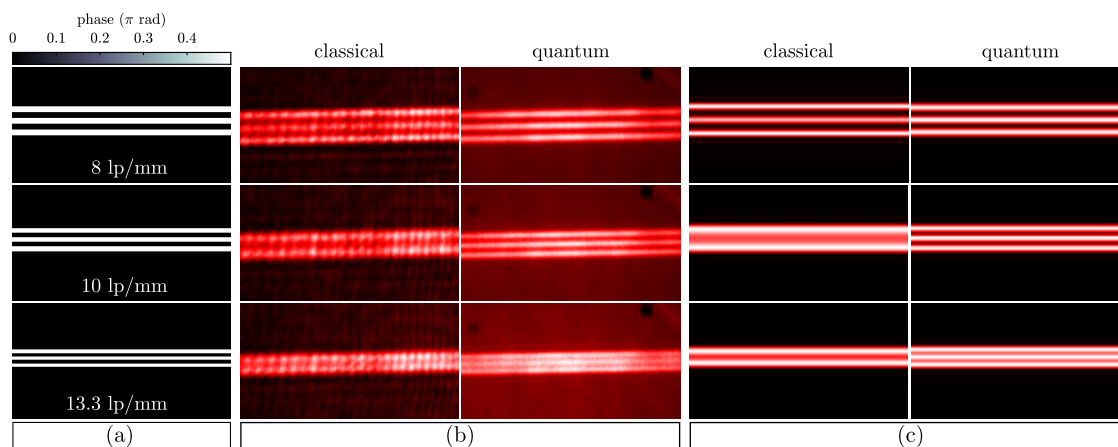


**Fig. 3.** Comparison of resolution between classical phase-shifting holography and quantum phase-shifting holography. (a) Object, a series of three horizontal bars with a maximum phase shift of  $\pi/2$  were used to measure resolution. The spatial frequency of the bars varied from 8 lp/mm (top row) to 10 lp/mm (middle row) to 13.3 lp/mm (bottom row). (b) Experimental results (interferograms) indicate that the three bars are clearly resolved in both the quantum and classical experiments at a spatial frequency of 8 lp/mm (top row). However, only the quantum phase-shifting holography scheme can resolve the bars at a spatial frequency of 10 lp/mm (middle row) and 13.3 lp/mm (bottom row). (c) A simulation of the experiments in Fig. 1 agrees very closely with the experimental results in (b). In (b) and (c), the intensity is normalized by the maximum intensity.

the three spatial frequencies used. Furthermore, the simulation also reproduces the decrease in visibility for the quantum experimental data at a spatial frequency of 13.3 lp/mm. The classical simulation [“classical” column, Fig. 3(c)] reproduces the loss of resolution in the classical experiment for both the 10 and 13.3 lp/mm data, whereby the three bars are only resolved as two bars. Quantum phase-shifting holography achieves a greater resolution than classical phase-shifting holography for the same imaging system because the two-photon field created in spontaneous parametric downconversion has a larger spatial bandwidth than the laser beam used in the classical experiment [33]. The spatial bandwidth of spontaneous parametric downconversion is primarily controlled by the length of the nonlinear crystal and can be evaluated by considering the marginal of  $|\psi_0(\kappa_s, \kappa_i)|^2$ . Because the phase object is probed with spatially broadband light in the quantum experiment, more high spatial frequency content passes through the bandwidth-limiting aperture. This effect is similar in origin to the increase in spatial resolution granted by structured-illumination microscopy [37].

## 5. CONCLUSION

We have demonstrated a phase-shifting holography method that relies upon the indistinguishability between photons produced in successive downconversion events in a nonlinear crystal. When compared to an equivalent low-light fully coherent classical phase-shifting holography system, our method achieves twice the phase shift and approximately 1.7 times the spatial resolution, in agreement with the numerical simulation. By doubling the phase shift imparted to light interacting with a phase-only object, we were able to obtain half the fractional uncertainty in a quantitative measurement of the phase imparted by that object. This increase in signal-to-noise has a clear benefit in low-light imaging of light sensitive biological cells and tissues, which typically suffers from background noise being of nearly the same intensity as the signal. At the same time, our method avoids coincidence imaging, which can require data collection times lasting several hours to achieve a comparable signal-to-noise ratio [8]. Our method requires only tens of seconds to collect all the data, which is much closer to the relevant time scale of biological imaging. Implementing our quantum phase-shifting holography technique in high numerical aperture imaging systems will require careful phase stabilization. Additionally, samples thicker than the biphoton birth zone in the nonlinear crystal or those with multiple scattering layers will produce a degraded phase image. It may be possible to achieve a higher spatial resolution by imaging the signal and idler photons in coincidence because the effective aperture experienced by the coincidence image is a convolution of the apertures for the individual signal and idler photons [35]. Furthermore, our scheme may be fundamentally more phase-sensitive than classical phase-shifting holography due to the Heisenberg scaling of phase uncertainty [38], and future work would involve testing this feature.

**Funding.** National Science Foundation (2138174); Office of Naval Research (N00014-20-1-2558); U.S. Department of Energy (FWP 76295); Natural Sciences and Engineering Research Council of Canada.

**Acknowledgment.** R. W. B. also acknowledges support through the Natural Sciences and Engineering Research Council of Canada, the Canada Research Chairs program, the Canada First Research Excellence Fund award on Transformative Quantum Technologies, by the U.S. Office of Naval Research, and by the U.S. National Science Foundation.

**Disclosures.** The authors declare no conflicts of interest.

**Data availability.** Data underlying the results presented in this paper are not publicly available at this time but may be obtained from the authors upon reasonable request.

**Supplemental document.** See Supplement 1 for supporting content.

## REFERENCES

1. F. Zernike, “How I discovered phase contrast,” *Science* **121**, 345–349 (1955).
2. G. Nomarski, “Microinterféromètre différentielle à ondes polarisées,” *J. Phys. Radium* **16**, 9 (1955).
3. J. H. Bruning, D. R. Herriott, J. E. Gallagher, D. P. Rosenfeld, A. D. White, and D. J. Brangaccio, “Digital wavefront measuring interferometer for testing optical surfaces and lenses,” *Appl. Opt.* **13**, 2693–2703 (1974).
4. I. Yamaguchi and T. Zhang, “Phase-shifting digital holography,” *Opt. Lett.* **22**, 1268–1270 (1997).
5. E. Cuhe, P. Marquet, and C. Depeursinge, “Spatial filtering for zero-order and twin-image elimination in digital off-axis holography,” *Appl. Opt.* **39**, 4070–4075 (2000).
6. R. S. Aspden, N. R. Gemmell, P. A. Morris, D. S. Tasca, L. Mertens, M. G. Tanner, R. A. Kirkwood, A. Ruggeri, A. Tosi, R. W. Boyd, G. S. Buller, R. H. Hadfield, and M. J. Padgett, “Photon-sparse microscopy: visible light imaging using infrared illumination,” *Optica* **2**, 1049–1052 (2015).
7. V. Giovannetti, S. Lloyd, L. Maccone, and J. H. Shapiro, “Sub-Rayleigh-diffraction-bound quantum imaging,” *Phys. Rev. A* **79**, 013827 (2009).
8. M. Reichert, H. Defienne, and J. W. Fleischer, “Massively parallel coincidence counting of high-dimensional entangled states,” *Sci. Rep.* **8**, 7925 (2018).
9. H. Defienne, M. Reichert, and J. W. Fleischer, “Adaptive quantum optics with spatially entangled photon pairs,” *Phys. Rev. Lett.* **121**, 233601 (2018).
10. A. N. Black, E. Giese, B. Braverman, N. Zollo, S. M. Barnett, and R. W. Boyd, “Quantum nonlocal aberration cancellation,” *Phys. Rev. Lett.* **123**, 143603 (2019).
11. N. H. Valencia, S. Goel, W. McCutcheon, H. Defienne, and M. Malik, “Unscrambling entanglement through a complex medium,” *Nat. Phys.* **16**, 1112–1116 (2020).
12. T. Aidukas, P. C. Konda, A. R. Harvey, M. J. Padgett, and P.-A. Moreau, “Phase and amplitude imaging with quantum correlations through Fourier ptychography,” *Sci. Rep.* **9**, 10445 (2019).
13. H. Defienne, B. Ndagano, A. Lyons, and D. Faccio, “Polarization entanglement-enabled quantum holography,” *Nat. Phys.* **17**, 591–597 (2021).
14. R. Camphausen, Á. Cuevas, L. Duempelmann, R. A. Terborg, E. Wajs, S. Tisa, A. Ruggeri, I. Cusini, F. Steinlechner, and V. Pruneri, “A quantum-enhanced wide-field phase imager,” *Sci. Adv.* **7**, eabj2155 (2021).
15. X. Y. Zou, L. J. Wang, and L. Mandel, “Induced coherence and indistinguishability in optical interference,” *Phys. Rev. Lett.* **67**, 318–321 (1991).
16. G. B. Lemos, V. Borish, G. D. Cole, S. Ramelow, R. Lapkiewicz, and A. Zeilinger, “Quantum imaging with undetected photons,” *Nature* **512**, 409–412 (2014).
17. J. H. Shapiro, D. Venkatraman, and F. N. C. Wong, “Classical imaging with undetected photons,” *Sci. Rep.* **5**, 10329 (2015).
18. A. C. Cardoso, L. P. Berruezo, D. F. Ávila, G. B. Lemos, W. M. Pimenta, C. H. Monken, P. L. Saldanha, and S. Pádua, “Classical imaging with undetected light,” *Phys. Rev. A* **97**, 033827 (2018).
19. I. Kviatkovsky, H. M. Chrzanowski, E. G. Avery, H. Bartolomeaus, and S. Ramelow, “Microscopy with undetected photons in the mid-infrared,” *Sci. Adv.* **6**, eabd0264 (2020).
20. A. V. Paterova, H. Yang, Z. S. D. Toa, and L. A. Krivitsky, “Quantum imaging for the semiconductor industry,” *Appl. Phys. Lett.* **117**, 054004 (2020).
21. A. V. Paterova, S. M. Maniam, H. Yang, G. Greci, and L. A. Krivitsky, “Hyperspectral infrared microscopy with visible light,” *Sci. Adv.* **6**, eabd0460 (2020).
22. B. E. Haase, J. Hennig, M. Kutas, E. Waller, J. Hering, G. von Freymann, and D. Molter, “Phase-quadrature quantum imaging with undetected photons,” *Opt. Express* **31**, 143–152 (2023).
23. D. A. Kalashnikov, A. V. Paterova, S. P. Kulik, and L. A. Krivitsky, “Infrared spectroscopy with visible light,” *Nat. Photonics* **10**, 98–101 (2016).

24. B. Viswanathan, G. B. Lemos, and M. Lahiri, "Resolution limit in quantum imaging with undetected photons using position correlations," *Opt. Express* **29**, 38185–38198 (2021).
25. Y. Niwa, T. Matsuo, K. Onai, D. Kato, M. Tachikawa, and M. Ishiura, "Phase-resetting mechanism of the circadian clock in *Chlamydomonas reinhardtii*," *Proc. Natl. Acad. Sci. USA* **110**, 13666–13671 (2013).
26. Q. Thommen, B. Pfeuty, P. Schatt, A. Bijoux, F.-Y. Bouget, and M. Lefranc, "Probing entrainment of *Ostreococcus tauri* circadian clock by green and blue light through a mathematical modeling approach," *Front. Genet.* **6**, 65 (2015).
27. H. Defienne, M. Reichert, and J. W. Fleischer, "General model of photon-pair detection with an image sensor," *Phys. Rev. Lett.* **120**, 203604 (2018).
28. M. Reichert, H. Defienne, and J. W. Fleischer, "Optimizing the signal-to-noise ratio of biphoton distribution measurements," *Phys. Rev. A* **98**, 013841 (2018).
29. T. Gregory, P.-A. Moreau, E. Toninelli, and M. J. Padgett, "Imaging through noise with quantum illumination," *Sci. Adv.* **6**, eaay2652 (2020).
30. P. A. Morris, R. S. Aspden, J. E. C. Bell, R. W. Boyd, and M. J. Padgett, "Imaging with a small number of photons," *Nat. Commun.* **6**, 5913 (2015).
31. O. Wolley, T. Gregory, S. Beer, T. Higuchi, and M. Padgett, "Quantum imaging with a photon counting camera," *Sci. Rep.* **12**, 8286 (2022).
32. D. Bouchet, J. Dong, D. Maestre, and T. Juffmann, "Fundamental bounds on the precision of classical phase microscopes," *Phys. Rev. Appl.* **15**, 024047 (2021).
33. G. Frascella, E. E. Mikhailov, N. Takanashi, R. V. Zakharov, O. V. Tikhonova, and M. V. Chekhova, "Wide-field  $su(1,1)$  interferometer," *Optica* **6**, 1233–1236 (2019).
34. E. Lantz, J.-L. Blanchet, L. Furfaro, and F. Devaux, "Multi-imaging and Bayesian estimation for photon counting with EMCCDs," *Mon. Not. R. Astron. Soc.* **386**, 2262–2270 (2008).
35. I. F. Santos, M. A. Sagiore, C. H. Monken, and S. Pádua, "Resolution and apodization in images generated by twin photons," *Phys. Rev. A* **67**, 033812 (2003).
36. J. W. Goodman, *Introduction to Fourier Optics* (Roberts and Company, 2005).
37. S. Chowdhury, A.-H. Dhalla, and J. Izatt, "Structured oblique illumination microscopy for enhanced resolution imaging of non-fluorescent, coherently scattering samples," *Biomed. Opt. Express* **3**, 1841–1854 (2012).
38. R. Nold, C. Babin, J. Schmidt, T. Linkewitz, M. T. P. Zaballos, R. Stöhr, R. Kolesov, V. Vorobyov, D. M. Lukin, R. Boppert, S. Barz, J. Vučković, J. C. M. Gebhardt, F. Kaiser, and J. Wrachtrup, "Quantum optical microphone in the audio band," *PRX Quantum* **3**, 020358 (2022).

**Authors' comments on the Supplemental Document to "Quantum-enhanced phase imaging without coincidence counting, A. N. Black et al., Optica 10, 952-958 (2023)."**

Several formatting errors were introduced into the Supplemental Document accompanying our article during the final production process. For example, symbols that belong on the baseline of an equation have been typeset as subscripts. As a result, this version, which is the version of record, is considerably less comprehensible than the authors' version, the version accepted by the journal. We have thus included both versions in this file. The authors' version follows the published version and is easily recognizable because the lines of this document are numbered.

## Quantum-enhanced phase imaging without coincidence counting: supplement

**A. NICHOLAS BLACK,<sup>1,\*</sup>  LONG D. NGUYEN,<sup>1</sup>  BORIS BRAVERMAN,<sup>2</sup> KEVIN T. CRAMPTON,<sup>3</sup> JAMES E. EVANS,<sup>3,4</sup> AND ROBERT W. BOYD<sup>1,5</sup> **

<sup>1</sup>*Department of Physics and Astronomy, University of Rochester, Rochester, New York 14627, USA*

<sup>2</sup>*QuEra Computing Inc., Boston, Massachusetts 02135, USA*

<sup>3</sup>*Pacific Northwest National Laboratory, Environmental Molecular Sciences Laboratory, Richland, Washington 99354, USA*

<sup>4</sup>*School of Biological Sciences, Washington State University, Pullman, Washington 99164, USA*

<sup>5</sup>*Department of Physics, University of Ottawa, Ottawa, Ontario K1N 6N5, Canada*

\*[ablack18@ur.rochester.edu](mailto:ablack18@ur.rochester.edu)

---

This supplement published with Optica Publishing Group on 19 July 2023 by The Authors under the terms of the [Creative Commons Attribution 4.0 License](https://creativecommons.org/licenses/by/4.0/) in the format provided by the authors and unedited. Further distribution of this work must maintain attribution to the author(s) and the published article's title, journal citation, and DOI.

Supplement DOI: <https://doi.org/10.6084/m9.figshare.22698538>

Parent Article DOI: <https://doi.org/10.1364/OPTICA.482926>

# Supplementary Material: Quantum-enhanced phase imaging without coincidence counting

## 1. INCREASED SPATIAL RESOLUTION OF IMAGING WITH LIGHT PRODUCED FROM SPDC

The signal and idler photons produced in SPDC are individually in a spatially incoherent state [1]. The spatial bandwidth of the signal and idler photons is dictated by the phase-matching function of the crystal [2], and generally a shorter crystal will result in the signal and idler having a larger spatial bandwidth. The resolution enhancement afforded by imaging with spatially incoherent illumination will be briefly summarized here, following the treatment by Goodman [3]. Incoherent imaging is mathematically described as the convolution of the point spread function for the imaging system with the intensity of the object to be imaged,

$$I_{\text{img}}(\vec{x}) = \int |h(\vec{\zeta} - \vec{x})|^2 I_{\text{obj}}(\vec{\zeta}) d\vec{\zeta}, \quad (\text{S1})$$

where  $h(\vec{\zeta})$  is the coherent impulse response of the imaging system. The convolution in Eq. (S1) takes places over the transverse spatial coordinates.  $I_{\text{img}}(\vec{x})$  and  $I_{\text{obj}}(\vec{\zeta})$  are the spatially-resolved intensities of the image and object, respectively. The coherent impulse response is related to the amplitude transfer function of the imaging system through a Fourier-transform relationship,

$$H(\vec{k}) = \mathcal{F}\{h(\vec{x})\} \quad (\text{S2})$$

By taking the Fourier transform of both sides of Eq. (S1), it is easy to examine the effect of the point spread function on the bandwidth of the image,

$$\mathcal{F}\{I_{\text{img}}(\vec{x})\} = \mathcal{F}\{|h(\vec{x})|^2\} \mathcal{F}\{I_{\text{obj}}(\vec{x})\}. \quad (\text{S3})$$

The Fourier transform of the point spread function, known as the optical transfer function, controls the bandwidth of the resulting image. Using the autocorrelation theorem of Fourier transforms, it is possible to express the optical transfer function in terms of the amplitude transfer function,

$$H_{\text{incoh}}(\vec{k}) = H(\vec{k}) * H(\vec{k}). \quad (\text{S4})$$

If the amplitude transfer function,  $H$ , has finite support, then its autocorrelation,  $H_{\text{incoh}}$ , will typically have support that is twice as large. Thus, imaging with incoherent illumination will usually yield twice the resolution, from a bandwidth perspective, than the same imaging scenario with coherent illumination. It should be noted that the increase in resolution garnered by incoherent illumination is usually only true when a real-valued object is imaged. However, if the phase is measured, spatially incoherent illumination will still yield an increase in resolution.

Figure S1 shows the effect of a bandwidth-limiting aperture in both (a) the classical and (b) the quantum phase imaging experiments. In both scenarios, a phase object of the form,

$$\phi_{\text{obj}}(x) = \frac{\pi}{2} (1 + \cos[k_{\text{grat}}x]) \quad (\text{S5})$$

is added in one arm of the interferometer, where  $k_{\text{grat}} = 2\pi/1.95\text{mm}^{-1}$ . The simulation is stopped 12.5 cm behind L5. At this position, transverse spatial frequency is mapped to position according to  $\vec{k} = k\vec{\zeta}/f$ , where  $\vec{\zeta}$  is the transverse position and  $f$  is the focal length of L5. Figure S1 shows the angular spectrum of the classical coherent field, where

$$E_{\text{grat}}(x) = E(x)h_1 + e^{i\phi_{\text{obj}}(x)}i. \quad (\text{S6})$$

$E(x)$  is a Gaussian beam of with a radius of 3 mm at the SLM plane, the location of the phase object in the interferometer. The spacing between the diffractive orders in Fig. S1 is a factor of

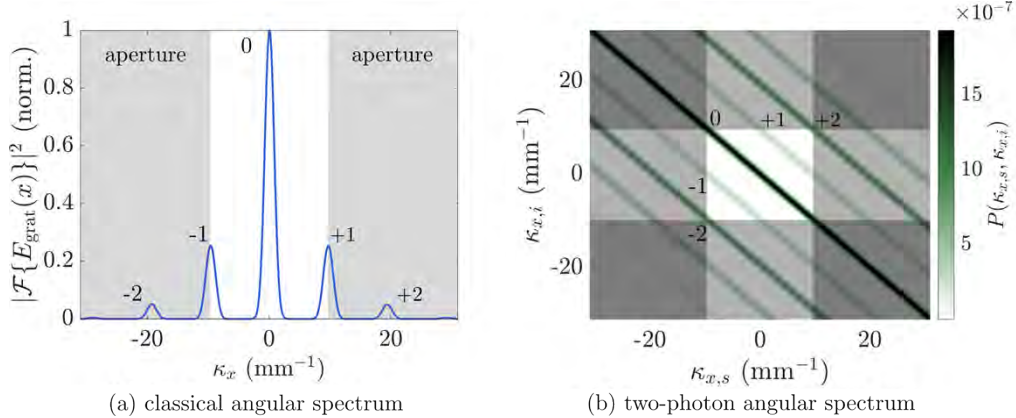


**Fig. S1.** The effect of a bandwidth-limiting aperture (overlaid in gray) on the (a) classical and (b) quantum phase imaging experiments. In the classical experiment, the aperture allows the 0 and half the  $\pm 1$  diffractive orders to pass (non-grey region). The same aperture placed in the path of the entangled signal and idler photons allows the 0, +1, and half the +2 diffractive orders to pass for an illuminating signal photon with a spatial frequency of  $\kappa_{x,s} = -3k_{\text{grat}}$ . For this particular signal photon's entangled idler at  $\kappa_{x,i} = 3k_{\text{grat}}$ , the 0, -1, and half the -2 diffractive orders pass through the aperture. A similar effect occurs for signal and idler pairs  $\kappa_{x,s} = -\kappa_{x,i} = 3k_{\text{grat}}$ .

three greater than  $k_{\text{grat}}$  because the image of the phase object is demagnified by a factor of 0.3 before passing through L5, like in the actual experiment. A bandwidth-limiting aperture is placed in the focal plane of L5 such that it blocks half the -1 and +1 diffractive orders in the classical field, grey overlay in Fig. S1(a).

In Fig. S1(b), the same bandwidth-limiting aperture is imposed upon the two-photon angular spectrum of the quantum experiment. The non-shaded portion of the two-photon angular spectrum represents the signal and idler spatial frequencies that pass through the aperture. For reference, the diffractive orders of one particular combination of signal and idler spatial frequencies,  $\kappa_{x,i} = -\kappa_{x,s} = 3k_{\text{grat}}$  are labeled. Note that because the signal and idler photons are anti-correlated in their spatial frequency, the spatial frequencies mentioned above correspond to a particular down-conversion event. For the signal spatial frequency at  $-3k_{\text{grat}}$ , the 0, +1, and half the +2 frequencies pass through the aperture. Similarly, for the corresponding idler photon at  $3k_{\text{grat}}$ , the 0, -1, and half the -2 diffractive orders pass through the aperture. Thus, by virtue of the wider spatial bandwidth of the illuminating signal and idler photons, the quantum experiment has a higher resolution than the classical experiment.

We note that the increased resolution of the quantum experiment is not necessarily a quantum effect, though the strong spatial correlations between the signal and idler are quantum in nature. The double phase shift leading to an increased signal-to-noise is rooted in both the quantum nature of the interference between successive down-conversion events and the spatial correlations of the signal and idler. In principle, one could use spatially broadband classical light to perform phase-shifting holography but would not achieve twice the phase shift. Furthermore, while "double-passing" a sample under observation with classical spatially broadband light would achieve a double phase shift, it would come at the cost of requiring a longer depth of focus, potentially decreasing the magnification of the imaging system. Illuminating the sample with spatially entangled photons from SPDC alleviates this requirement because the sample can be imaged with twice the phase shift in a single pass.

## REFERENCES

1. P. H. S. Ribeiro, C. H. Monken, and G. A. Barbosa, "Measurement of coherence area in parametric downconversion luminescence," *Appl. Opt.* **33**, 352–355 (1994).
2. G. Frascella, E. E. Mikhailov, N. Takanashi, R. V. Zakharov, O. V. Tikhonova, and M. V. Chekhova, "Wide-field su(1,1) interferometer," *Optica* **6**, 1233–1236 (2019).
3. J. W. Goodman, *Introduction to Fourier optics* (Roberts and Company, 2005).

# Supplementary Material: Quantum-enhanced phase imaging without coincidence counting

A. NICHOLAS BLACK,<sup>1,\*</sup> LONG D. NGUYEN,<sup>1</sup> BORIS BRAVERMAN,<sup>2</sup>  
KEVIN T. CRAMPTON,<sup>3</sup> JAMES E. EVANS,<sup>3,4</sup> AND ROBERT W.  
BOYD<sup>1,5</sup>

<sup>1</sup>*Department of Physics and Astronomy, University of Rochester, Rochester, NY 14627, USA*

<sup>2</sup>*QuEra Computing Inc., Boston, MA 02135, USA*

<sup>3</sup>*Pacific Northwest National Laboratory, Environmental Molecular Sciences Laboratory, Richland, WA 99354, USA*

<sup>4</sup>*School of Biological Sciences, Washington State University, Pullman, WA 99164, USA*

<sup>5</sup>*Department of Physics, University of Ottawa, Ottawa, ON K1N 6N5, Canada*

\*[ablack18@ur.rochester.edu](mailto:ablack18@ur.rochester.edu)

## 1. Increased Spatial Resolution of Imaging with Light Produced from SPDC

The signal and idler photons produced in SPDC are individually in a spatially incoherent state [1]. The spatial bandwidth of the signal and idler photons is dictated by the phase-matching function of the crystal [2], and generally a shorter crystal will result in the signal and idler having a larger spatial bandwidth. The resolution enhancement afforded by imaging with spatially incoherent illumination will be briefly summarized here, following the treatment by Goodman [3]. Incoherent imaging is mathematically described as the convolution of the point spread function for the imaging system with the intensity of the object to be imaged,

$$I_{\text{img}}(\mathbf{x}) = \int |h(\boldsymbol{\xi} - \mathbf{x})|^2 I_{\text{obj}}(\boldsymbol{\xi}) d\boldsymbol{\xi}, \quad (1)$$

where  $h(\boldsymbol{\xi})$  is the coherent impulse response of the imaging system. The convolution in Eq. (1) takes places over the transverse spatial coordinates.  $I_{\text{img}}(\mathbf{x})$  and  $I_{\text{obj}}(\boldsymbol{\xi})$  are the spatially-resolved intensities of the image and object, respectively. The coherent impulse response is related to the amplitude transfer function of the imaging system through a Fourier-transform relationship,

$$H(\boldsymbol{\kappa}) = \mathcal{F}\{h(\mathbf{x})\} \quad (2)$$

By taking the Fourier transform of both sides of Eq. (1), it is easy to examine the effect of the point spread function on the bandwidth of the image,

$$\mathcal{F}\{I_{\text{img}}(\mathbf{x})\} = \mathcal{F}\{|h(\mathbf{x})|^2\} \mathcal{F}\{I_{\text{obj}}(\mathbf{x})\}. \quad (3)$$

The Fourier transform of the point spread function, known as the optical transfer function, controls the bandwidth of the resulting image. Using the autocorrelation theorem of Fourier transforms, it is possible to express the optical transfer function in terms of the amplitude transfer function,

$$H_{\text{incoh}}(\boldsymbol{\kappa}) = H(\boldsymbol{\kappa}) * H(\boldsymbol{\kappa}). \quad (4)$$

If the amplitude transfer function,  $H$ , has finite support, then its autocorrelation,  $H_{\text{incoh}}$ , will typically have support that is twice as large. Thus, imaging with incoherent illumination will usually yield twice the resolution, from a bandwidth perspective, than the same imaging scenario with coherent illumination. It should be noted that the increase in resolution garnered by incoherent illumination is usually only true when a real-valued object is imaged. However, if the phase is measured, spatially incoherent illumination will still yield an increase in resolution.

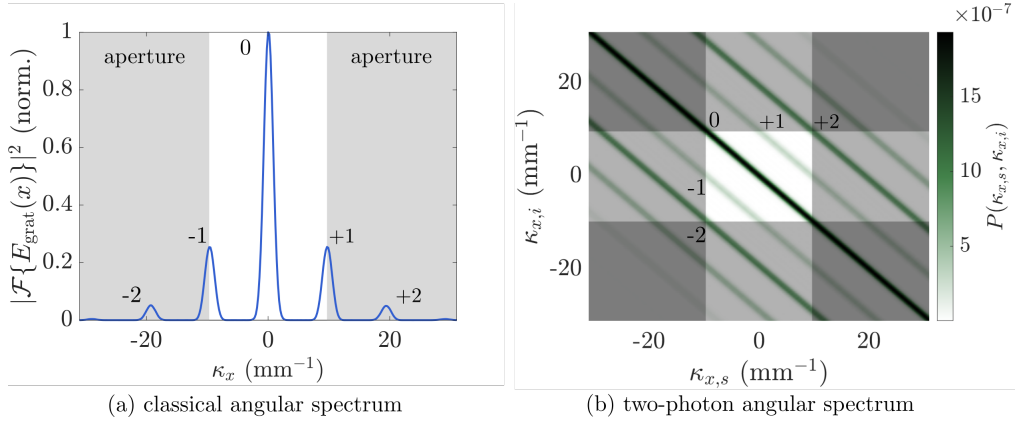


Fig. 1. The effect of a bandwidth-limiting aperture (overlaid in gray) on the (a) classical and (b) quantum phase imaging experiments. In the classical experiment, the aperture allows the 0 and half the  $\pm 1$  diffractive orders to pass (non-grey region). The same aperture placed in the path of the entangled signal and idler photons allows the 0, +1, and half the +2 diffractive orders to pass for an illuminating signal photon with a spatial frequency of  $\kappa_{x,s} = -3k_{\text{grat}}$ . For this particular signal photon's entangled idler at  $\kappa_{x,i} = 3k_{\text{grat}}$ , the 0, -1, and half the -2 diffractive orders pass through the aperture. A similar effect occurs for signal and idler pairs  $\kappa_{x,s} = -\kappa_{x,i} = 3k_{\text{grat}}$ .

36 Figure 1 shows the effect of a bandwidth-limiting aperture in both (a) the classical and (b) the  
 37 quantum phase imaging experiments. In both scenarios, a phase object of the form,

$$\phi_{\text{obj}}(x) = \frac{\pi}{2} (1 + \cos [k_{\text{grat}}x]) \quad (5)$$

38 is added in one arm of the interferometer, where  $k_{\text{grat}} = 2\pi/1.95\text{mm}^{-1}$ . The simulation is stopped  
 39 12.5 cm behind L5. At this position, transverse spatial frequency is mapped to position according  
 40 to  $\kappa = k\xi/f$ , where  $\xi$  is the transverse position and  $f$  is the focal length of L5. Figure 1 shows  
 41 the angular spectrum of the classical coherent field, where

$$E_{\text{grat}}(x) = E(x) \left[ 1 + e^{i\phi_{\text{obj}}(x)} \right]. \quad (6)$$

42  $E(x)$  is a Gaussian beam of with a radius of 3 mm at the SLM plane, the location of the phase  
 43 object in the interferometer. The spacing between the diffractive orders in Fig. 1 is a factor of  
 44 three greater than  $k_{\text{grat}}$  because the image of the phase object is demagnified by a factor of 0.3  
 45 before passing through L5, like in the actual experiment. A bandwidth-limiting aperture is placed  
 46 in the focal plane of L5 such that it blocks half the -1 and +1 diffractive orders in the classical  
 47 field, grey overlay in Fig. 1(a).

48 In Fig. 1(b), the same bandwidth-limiting aperture is imposed upon the two-photon angular  
 49 spectrum of the quantum experiment. The non-shaded portion of the two-photon angular  
 50 spectrum represents the signal and idler spatial frequencies that pass through the aperture.  
 51 For reference, the diffractive orders of one particular combination of signal and idler spatial  
 52 frequencies,  $\kappa_{x,i} = -\kappa_{x,s} = 3k_{\text{grat}}$  are labeled. Note that because the signal and idler photons are  
 53 anti-correlated in their spatial frequency, the spatial frequencies mentioned above correspond to a  
 54 particular down-conversion event. For the signal spatial frequency at  $-3k_{\text{grat}}$ , the 0, +1, and half  
 55 the +2 frequencies pass through the aperture. Similarly, for the corresponding idler photon at  
 56  $3k_{\text{grat}}$ , the 0, -1, and half the -2 diffractive orders pass through the aperture. Thus, by virtue of  
 57 the wider spatial bandwidth of the illuminating signal and idler photons, the quantum experiment  
 58 has a higher resolution than the classical experiment.

59 We note that the increased resolution of the quantum experiment is not necessarily a quantum  
60 effect, though the strong spatial correlations between the signal and idler are quantum in nature.  
61 The double phase shift leading to an increased signal-to-noise is rooted in both the quantum  
62 nature of the interference between successive down-conversion events and the spatial correlations  
63 of the signal and idler. In principle, one could use spatially broadband classical light to perform  
64 phase-shifting holography but would not achieve twice the phase shift. Furthermore, while  
65 "double-passing" a sample under observation with classical spatially broadband light would  
66 achieve a double phase shift, it would come at the cost of requiring a longer depth of focus,  
67 potentially decreasing the magnification of the imaging system. Illuminating the sample with  
68 spatially entangled photons from SPDC alleviates this requirement because the sample can be  
69 imaged with twice the phase shift in a single pass.

## 70 **References**

- 71 1. P. H. S. Ribeiro, C. H. Monken, and G. A. Barbosa, "Measurement of coherence area in parametric downconversion  
72 luminescence," *Appl. Opt.* **33**, 352–355 (1994).
- 73 2. G. Frascella, E. E. Mikhailov, N. Takanashi, R. V. Zakharov, O. V. Tikhonova, and M. V. Chekhova, "Wide-field  
74  $su(1,1)$  interferometer," *Optica* **6**, 1233–1236 (2019).
- 75 3. J. W. Goodman, *Introduction to Fourier optics* (Roberts and Company, 2005).